Direct imaging of molecular rotation with high-order-harmonic generation

Yanqing He,[1] Lixin He,[1] Pengfei Lan,[1,*] Baoning Wang,[1] Liang Li,[1] Xiaosong Zhu,[1] Wei Cao,[1] and Peixiang Lu[1,2,†]

[1]*Wuhan National Laboratory for Optoelectronics and School of Physics, Huazhong University of Science and Technology,*
Wuhan 430074, China
[2]*Hubei Key Laboratory of Optical Information and Pattern Recognition, Wuhan Institute of Technology, Wuhan 430205, China*

Direct imaging of molecular dynamics is a long-standing goal in physics and chemistry. As an emerging tool, high-order-harmonic spectroscopy (HHS) enables accessing molecular dynamics on femtosecond to attosecond time scales. However, decoding information from the harmonic signals is usually painstaking due to the coherent nature of high-order-harmonic generation (HHG). Here we show that this obstacle can be effectively overcome by exploiting machine learning in HHS. Combining the machine learning with an angle-resolved HHS method, the molecular movie with femtosecond resolution is reconstructed from the angular distributions of HHG measured at various time delays of the probe pulse. Such a movie distinctly shows the full information of the coherent rotational dynamics of molecules, which is unattained in previous studies. The experimental retrievals are in good agreement with the numerical simulations. Our findings provide a comprehensive picture of molecular rotation in space and time, which will facilitate the development of related research on molecular dynamics imaging.

I. INTRODUCTION

Resolving molecular dynamics in time and space, viz., making a "molecular movie", has been long desired for its potential in revealing the intermediate processes of chemical reactions and biological transformations [1–3]. This enticing prospect, however, has encountered grand challenges over the last century due to the formidable spatiotemporal scales of molecular dynamics [4–7]. Recent advances in strong-field physics suggest that laser-driven electron-ion recollision [8–11] offers new opportunities for probing molecular dynamics with table-top lasers [12–19]. In particular, high-order-harmonic generation (HHG) from molecules encodes rich information on the molecular structure and dynamics, which has stimulated the development of high-order-harmonic spectroscopy (HHS) as an emerging tool for ultrafast molecular detection. In HHS, the temporal resolution comes from the interval between ionization and recombination events, and the spatial resolution is related to the de Broglie wavelength of the recombining electron, which promises resolving molecular dynamics on attosecond time scales [20–24] and imaging molecular structure with Ångstrom spatial resolution [25–27]. However, despite these superiorities, HHS also encounters rigorous challenges in the information decoding from the HHG signals. Especially for the complex-valued molecular information, of which both the amplitude and phase are coherently embroiled in the harmonic spectrum, the decoding is rather arduous or even unattainable [27,28]. In previous works on HHS, the phase information of the dynamics is either left out [29,30] or addressed based on the simulations or certain

approximations [25,31], which makes it very challenging to make a full molecular movie.

In recent years, with the emergence of artificial intelligence, the modern machine learning community has developed techniques with remarkable abilities to recognize, classify, and characterize complex sets of data with a high degree of accuracy, which have been widely applied in diverse domains, e.g., image processing [32,33], face recognition [34], and optical tomography [35]. More recently, machine learning has been explored as a tool in genetics [36], condensed-matter physics [37], and material science [38].

In this paper, we demonstrate the application of machine learning in HHS to probe molecular rotational dynamics with high resolution and fidelity. Molecular rotational control by coherently manipulating the rotational wave packet (RWP) has been proved an efficient way to connect the molecular and laboratory frames [39–43], which is significant for molecular structure imaging [25–27] and chemical reaction steering [22,44]. In experiment, the molecular frame dynamics is usually convolved with the rotational distribution of molecules in the laboratory. A thorough knowledge of molecular rotation in space and time therefore is a prerequisite for resolving the molecular frame dynamics from the measurement. However, decoding the molecular dynamics from the experimental observations is a challenging task. In previous studies, molecular rotation is usually cursorily described by the degree of molecular alignment [i.e., the mean values of the square or higher order of $\cos\theta$, where θ is the angle between the molecular axis and the pump laser (see below)] [39–41]. It is unable to reveal the full information of molecular RWP and to reconstruct the movie of molecular coherent rotation. Here by using an angle-resolved HHS method, we show that the rotational dynamics of the molecular RWP excited by a pump pulse is recorded in the angular distributions (ADs) of HHG

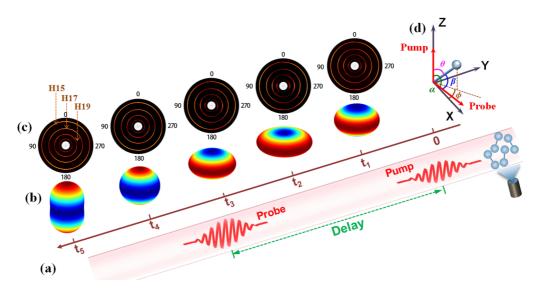*pengfeilan@mail.hust.edu.cn
†lupeixiang@mail.hust.edu.cn

FIG. 1. (a) Schematic diagram of the experimental scheme. The first pump pulse polarized along the z axis is applied at $t = 0$ to excite the molecular RWP. The subsequent probe pulse with adjustable time delay is applied to interact with the molecules to generate high-order harmonics. The harmonic ADs at each time delay are measured by scanning the polarization direction of the probe pulse in the xz plane [as illustrated in (d)]. (b) Illustration of the three-dimensional RWPs simulated at different time delays. (c) Illustration of the angle-resolved harmonic spectra measured at the time delays in (b). (d) Sketch of the geometry in our experiment.

measured at various polarization directions and time delays of the probe pulse. The time-dependent angular probability density of the RWP is then retrieved from the measured harmonic ADs by using a machine learning algorithm, which provides a full movie of the spatiotemporal evolution of the molecular RWP. The underlying mechanism of the molecular rotational dynamics is further revealed by analyzing the populations and phases of the excited rotational states. All the experimental retrievals agree well with the numerical simulations of the time-dependent Schrödinger equation (TDSE).

II. RESULTS AND DISCUSSION

HHG through laser-molecule interaction occurs under a much faster time scale than molecular rotation. The instantaneous rotational state of molecules can be encoded in the generated harmonic spectra. Our scheme for a molecular rotation movie is sketched in Fig. 1(a). Briefly, a pump pulse with moderate intensity, linearly polarized along the z axis [see the geometry in Fig. 1(d)], is first applied to the molecular ensemble to create molecular RWP through the stimulated Raman transitions [39]. Subsequently, an intense linearly polarized probe pulse with adjustable time delay is applied to interact with the excited molecules to generate high-order harmonics (for more experimental details, see Appendix A). Impulsively excited by the pump pulse, the molecules are temporarily well confined in a narrow cone around the polarization direction of the pump pulse (i.e., the z axis). Afterward, the created RWP disperses and evolves under the field-free condition as illustrated in Fig. 1(b). To characterize the spatial distribution of the molecular RWP, we measure the angular distributions (ADs) of the generated harmonics by scanning the polarizing angle α of the probe pulse with respect to the pump pulse in the xz plane spanned by the field vectors of these two pulses [see Fig. 1(d)]. The temporal evolution of molecular

RWP is traced by repeating this process at various time delays of the probe pulse. The time-dependent harmonics ADs then provide a series of snapshots of the molecular RWP during the evolution [see Fig. 1(c)]. The measurement at each time delay will make a "frame" in the "movie" of the evolution of molecular RWP.

To demonstrate our scheme, we choose the commonly used nitrogen (N_2) molecule as a prototype to do the HHG experiment. Figure 2(a) shows the measured time-dependent
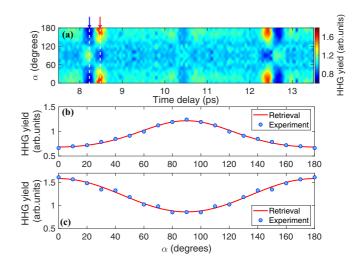

FIG. 2. (a) ADs of H17 as a function of the time delay of the probe pulse. Here, the harmonic yields have been normalized by the result of an unexcited ensemble (i.e., without the pump pulse). Results (dots) were measured at the time delay of (b) 8.2 ps [antialignment revival, as indicated by the blue arrow in (a)] and (c) 8.45 ps [alignment revival, as indicated by the red arrow in (a)]. The red lines in (b) and (c) show the reconstructions with the retrieved MAD $\rho(\theta, \phi, t)$.

ADs of harmonic 17 (H17) from N_2. The harmonic ADs show strong delay dependence at the rotational revivals, e.g., around $t = 8.4$ ps ($1T_{rev}$, $T_{rev} = \frac{1}{2B_0 c}$ is the revival period of N_2 with B_0 the rotational constant and c the velocity of light) and 12.6 ps ($1.5T_{rev}$). In Figs. 2(b) and 2(c), we plot the results (dots) measured at $t = 8.2$ and 8.45 ps [indicated by the blue and red arrows in Fig. 2(a)], respectively. One can see that the angle-dependent HHG yields measured at $t = 8.2$ ps exhibit a maximum at $\alpha = 90°$. Driven by a linearly polarized probe pulse, HHG from N_2 is most pronounced when the laser is parallel to the molecular axis due to the σ_g symmetry of the highest occupied molecular orbital (HOMO) of N_2 [45,46]. The maximal HHG yield at $\alpha = 90°$ in Fig. 2(b) implies that most molecules are aligned perpendicularly to the pump pulse, which just corresponds to an antialignment revival at $t = 8.2$ ps. While at $t = 8.45$ ps, the maximal HHG yield appears at $\alpha = 0°$ (or $180°$) where the probe pulse is parallel to the pump pulse, indicating an alignment revival at this moment. From the time-dependent harmonic ADs, the rapid quantum transformation of the molecular RWP from antialignment to alignment is directly identified. However, it is important to note that the measured harmonic AD is not an honest presentation of the distribution of molecular RWP, since the orientation-dependent electronic response is also convoluted in the HHG signals. For instance, at the same revivals (alignment or antialignment), HHG from a CO_2 molecule shows different ADs from N_2 (see Appendix B). To gain a molecular movie of the evolution of molecular RWP, a further decoding from the measured harmonic signals is required.

After the excitation of the pump pulse, the evolution of the RWP created from each initially populated rotational state $|JM\rangle$ [the eigenstate of the field-free rigid rotor described by the spherical harmonic $Y_J^M(\theta, \phi)$] can be expanded as [47]

$$\Psi_{JM}(\theta, \phi, t) = \sum_{J'M'} C_{JM,J'M'}(t) Y_{J'}^{M'}(\theta, \phi), \quad (1)$$

where $C_{JM,J'M'}(t) = |C_{JM,J'M'}(t)| e^{i\varphi_{JM,J'M'}(t)}$ is the time-dependent complex coefficient of each rotational eigenstate with the amplitude $|C_{JM,J'M'}(t)|$ and phase $\varphi_{JM,J'M'}(t)$. The labels J (or J') and M (or M') are associated with the total angular momentum and its projection onto the space-fixed z axis. Assuming a thermal distribution of the initial rotational states, the time-dependent molecular axis distribution (MAD) $\rho(\theta, \phi, t)$, which directly reflects the molecular rotational dynamics after the interaction of the molecular ensemble with the pump pulse, can be written as a weighted average of the modulus squares of the wave packet $\Psi_{JM}(\theta, \phi, t)$ [39,47–51], i.e.,

$$\rho(\theta, \phi, t) = \sum_{JM} \Gamma_{JM} |\Psi_{JM}(\theta, \phi, t)|^2, \quad (2)$$

where Γ_{JM} is the statistical weight (i.e., the population) of the initial state $|JM\rangle$ given by the Boltzmann distribution. HHG from the impulsively excited molecular ensemble can be related to the single-molecule contribution through the time-dependent MAD $\rho(\theta, \phi, t)$. Considering the coherent nature of HHG, the time-dependent harmonic ADs will thus
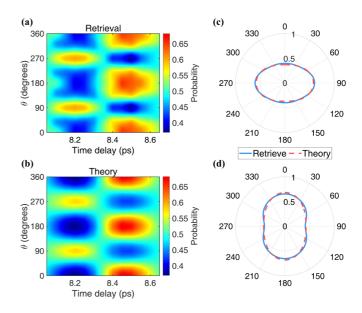

FIG. 3. (a) MAD $\rho(\theta, \phi, t)$ retrieved from the experiment. (b) Same as (a), but for the calculation result. Excited by the linearly polarized pump laser, the MAD $\rho(\theta, \phi, t)$ is ϕ independent. Plots (a) and (b) are just for the result of $\phi = 0°$. (c) and (d) show the polar plots of the retrieved (solid line) and calculated (dashed line) MADs $\rho(\theta, \phi, t)$ at the time delay of 8.2 ps (antialignment revival) and 8.45 ps (alignment revival), respectively.

be given by [50,51]

$$I_q(\alpha, t) = \left| \int_{\phi=0}^{2\pi} \int_{\theta=0}^{\pi} S_q(\beta) \rho(\theta, \phi, t) \sin\theta \, d\theta \, d\phi \right|^2. \quad (3)$$

Here θ and ϕ are the polar and azimuthal angles of molecular axis with respect to the z and x axes [see Fig. 1(d)]. β is the angle between the molecular axis and the polarization of the probe laser, which obeys $\cos\beta = \sin\theta \sin\alpha \cos\phi + \cos\theta \cos\alpha$. $S_q(\beta)$ is the induced dipole moment of the qth harmonic related to the single-molecule response with given orientation. In our reconstruction, we calculate the single-molecule dipole moment $S_q(\beta)$ by using the quantitative rescattering (QRS) theory [10,51], of which the accuracy and validity in modeling molecular HHG have been well established. Equations (1)–(3) set up a function between the harmonic ADs $I_q(\alpha, t)$ and the complex coefficients $C_{JM,J'M'}(t)$. The reconstruction of the molecular rotation movie requires the retrieval of the complex coefficients (both amplitude and phase) for all the relevant initial states from the measured harmonic ADs. To this end, we introduce machine learning to the HHS study, and employ a global optimization algorithm—the simulated annealing (SA) algorithm (see Appendix C), which is an efficient solver for approximating the global optimum of a given function in a large search space—to do the retrieval.

In Figs. 2 and 3, we have recuperated the time-dependent MAD $\rho(\theta, \phi, t)$ as well as the harmonic ADs $I_q(\alpha, t)$ in terms of Eqs. (2) and (3) by using the retrieved coefficients $C_{JM,J'M'}$. As shown in Figs. 2(b) and 2(c), the recuperated harmonic ADs (solid lines) are in excellent agreement with experimental data (dots), indicating a high accuracy of the SA algorithm. In Fig. 3(a), we show the recuperated MAD $\rho(\theta, \phi, t)$. Note that imposed by the linearly polarized pump pulse, the resulting
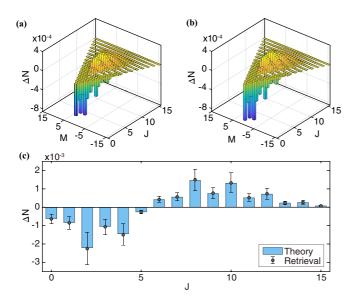
FIG. 4. (a) Change of the rotational-state population retrieved from the experiment data. (b) Same as (a), but for the calculation results. (c) Population change of the J states obtained by summing up the individual M state contributions. The bars and dots are for the calculated and retrieved results, respectively. Here, the error bars represent the standard deviation of the retrievals at different time delays.

FIG. 5. (a) Time-dependent phases (dots) of the rotational eigenstates Y_0^0, Y_2^0, and Y_4^0 retrieved for the initial state $|00\rangle$. Dashed lines show the linear fitting of the retrievals. (b) Same as (a), but for the rotational eigenstates Y_1^0, Y_3^0, and Y_5^0 from the initial state $|10\rangle$.

RWP has a cylindrical symmetry in space, thus $\rho(\theta, \phi, t)$ is independent of the azimuthal angle ϕ [39,47]. Figure 3 just shows the result of $\phi = 0°$. From Fig. 3(a), one can see clear signatures of the antialignment and alignment revivals at $t = 8.2$ and 8.45 ps, respectively. To evaluate the quality of the retrievals, we have theoretically calculated the MAD $\rho(\theta, \phi, t)$ by solving the TDSE of molecular RWP (see Appendix D). In our calculations, the laser intensity of the pump pulse has been optimized so that the squared difference between the measured and calculated signals is minimal. The calculated results are shown in Fig. 3(b). It is evident that the main distribution of the experimental retrieval agrees well with the theoretical one. For better comparison, the retrieved (solid line) and calculated (dashed line) results at the time delays of 8.2 and 8.45 ps are also presented in Figs. 3(c) and 3(d). The overall agreement between the retrievals (solid line) and calculations (dashed line) are excellent.

A deep insight into this rich rotational dynamics is further revealed by analyzing the amplitude and phase of the RWP created from each initial rotational states. The amplitude is associated with the populations of the rotational states. Excited by the pump pulse, the populations of the contributing rotational states are redistributed due to the transitions between different states. The rotational transition induced by the pump pulse can be quantified by analyzing the population change $\Delta N_{JM} = N_{JM} - \Gamma_{JM}$ of each rotational state. Here, $N_{JM} = \sum_{J'M'} \Gamma_{J'M'} |C_{J'M',JM}|^2$ represents the population of the rotational state $|JM\rangle$ after the excitation of the pump pulse. Figure 4(a) depicts the ΔN retrieved from the experiment. Note that after the impulsive excitation of the pump pulse, the created RWP evolves field-freely. The population N_{JM} is almost ti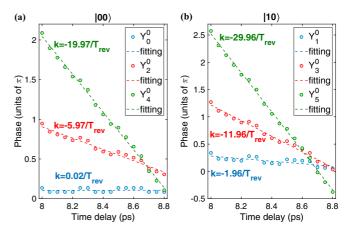me-delay independent. The result in Fig. 4(a) is an average of the retrievals at different time delays. It is clear that excited by the pump pulse, the lower-lying rotational states are transferred to much higher rotational levels. Owing to the linear polarization of the pump pulse, the magnetic quantum number M is conserved in the transitions, i.e., $\Delta M = 0$. Since the lower-lying rotational states possess smaller magnetic quantum number M, the populations of high rotational states are mainly concentrated at small M states. Moreover, the distribution over the magnetic quantum number M after the interaction is symmetric, agreeing with the cylindrical symmetry of the excitation. These results are consistent with the theoretical calculations shown in Fig. 4(b). For a direct comparison with the theory, we count up the populations of the sub-M states for each J state. As shown in Fig. 4(c), regardless of the experimental error, the agreement between the experiment (dots) and theory (bars) is excellent.

In Fig. 5, we show the retrieved phase $\varphi_{JM,J'M'}$ of the relevant rotational states as a function of the pump-probe delay. Figure 5(a) depicts the results of the rotational eigenstates Y_0^0, Y_2^0, and Y_4^0 created from the initial $|00\rangle$ state. It is obvious that the retrieved phase of each rotational eigenstate (dots) exhibits a nearly linear change with the time delay. Dotted curves in Fig. 5 show the linear fitting of these retrievals. The slopes (as indicated) of the fitting curves are very close to $-\frac{E_J}{\hbar}$, where $E_J = 2\pi\hbar B_0 c J(J+1) = \pi\hbar J(J+1)/T_{rev}$ is the eigenenergy of the considered rotational eigenstates. This result is consistent with the field-free nature of the evolution of the RWP after the interaction, which is described by a phase factor $e^{-i\frac{E_J}{\hbar}t}$ [39,47]. With the complex coefficients $C_{JM,J'M'}$ retrieved, we can then reproduce the dynamics of the RWP created from each initial rotational state in terms of Eq. (1). Figures 6(a)–6(d) display some selected snapshots of the RWP created from the $|00\rangle$, $|10\rangle$, $|20\rangle$, and $|30\rangle$ states, respectively. One can see that, owing to the time-dependent phase beating of the coherently populated rotational eigenstates, the RWPs created from different initial rotational states at the rotation revivals are synchronously condensed or stretched along the z axis, thus leading to the oblate or prolate angular distribution of molecules at the antialignment or alignment
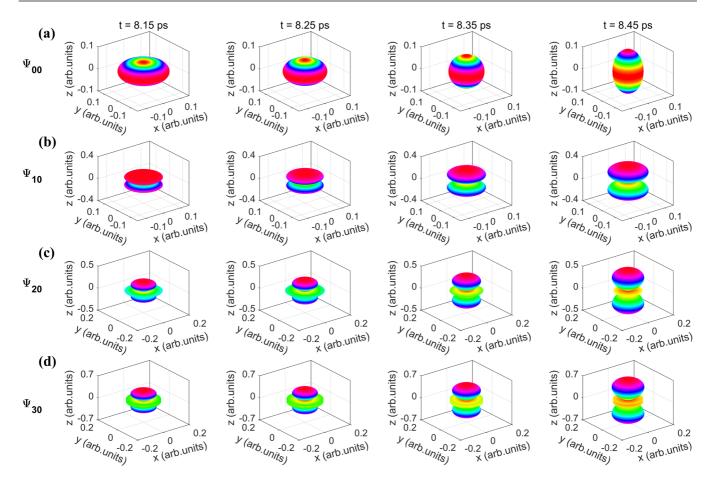
FIG. 6. Reconstructions of the RWPs created from different initial states. (a) Spatiotemporal evolution of the RWP reconstructed for the initial state $|00\rangle$. (b)–(d) Same as (a), but for the initial states $|10\rangle$, $|20\rangle$, and $|30\rangle$, respectively.

revival. Through a thermal average over these created RWPs, a complete movie of molecular rotational dynamics then is achieved (see the movie in the Supplemental Material [52]).

III. CONCLUSION

In summary, we demonstrate a full experimental reconstruction of molecular rotational dynamics by using an angle-resolved HHS method in combination with the machine learning algorithm. Excited by a pump pulse, the subsequent evolution of coherent molecular RWP is monitored by measuring the harmonic ADs at various time delays of the probe pulse. Utilizing a machine learning algorithm, a full movie of the evolution of molecular RWP in space and time is successfully retrieved from the measured harmonic ADs. The experimental retrievals agree well with the TDSE simulations. The present results afford a thoroughgoing knowledge of the spatiotemporal evolution of the field-free molecular RWP, which is useful for future research on ultrafast imaging of strong-field molecular frame dynamics.

On the other hand, machine learning provides a practical and robust method for extracting information from the HHG spectra. It is general and can be effectively extended to other molecules such as CO_2 (see Appendix B) and even some more complex polyatomic molecules. Moreover, HHG from molecules also contains abundant information on the electronic structure and dynamics. The exploitation of machine

learning in HHS could also open access to the ultrafast charge migration in molecules. In the future, machine learning is expected to be an extremely effective technique in attosecond physics for "watching" a chemical reaction.
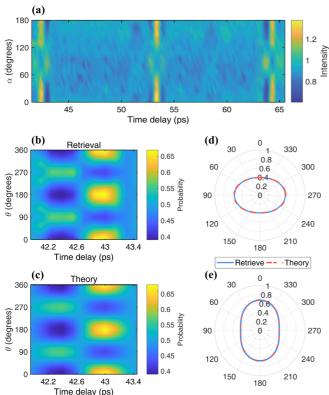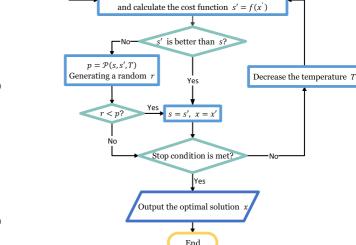
APPENDIX A: EXPERIMENTAL DETAILS

Our experiment is carried out by using a commercial Ti:sapphire laser system (Astrella-USP-1K, Coherent, Inc.), which delivers 35-fs, 800-nm pulses at a repetition rate of 1 kHz. The output laser is split by a beam splitter to produce the pump and probe pulses. The pump pulse polarized along the z axis is first used to create molecular RWP. Subsequently, the intense probe pulse with adjustable time delay is applied to interact with the molecule ensemble to generate

(a)

(b) Retrieval

(d)

(c) Theory

(e)

Retrieve —— · Theory - - -

FIG. 7. (a) ADs of H25 from CO_2 as a function of the time delay of the probe pulse. Here, the harmonic yields have been normalized by the result of the unexcited ensemble. (b) MAD $\rho(\theta, \phi, t)$ retrieved from the experiment data. (c) Same as (b), but for the calculation result. (d) and (e) show the polar plots of the retrieved (solid line) and calculated (dashed line) MADs $\rho(\theta, \phi, t)$ at the time delay of 42.4 ps (antialignment revival) and 43 ps (alignment revival), respectively.

high-order harmonics. A motorized delay line and a half-wave plate are installed in the arm of the probe pulse to adjust its time delay and polarization with respect to the pump one. These two beams are focused to a gas jet (500-μm diameter) by a 300-mm focal-length lens. The gas pressure is maintained at 20 Torr and the rotational temperature is estimated to be about 100 K [53]. The generated harmonic spectrum is detected by a homemade flat-field soft x-ray spectrometer [54].

APPENDIX B: EXPERIMENTAL RETRIEVALS OF CO_2 MOLECULE

To demonstrate the generality of our scheme, we have also performed a HHG experiment with the CO_2 molecule. Figure 7(a) shows the measured time-dependent harmonic ADs of H25 from the CO_2 molecule. Similar to N_2, one can also see strong delay dependence of the harmonic ADs at the rotational revivals (e.g., around $t = 42.4$, 53.35, and 64.3 ps). From the measured harmonic ADs, we have also retrieved the rotational dynamics of the CO_2 molecule with the same procedure as N_2. Figure 7(b) shows the recuperated time-dependent MAD $\rho(\theta, \phi, t)$ of CO_2, from which one can see clear signatures of the antialignment and alignment revivals at 42.4 and 43 ps, respectively. The TDSE simulations are also presented in Fig. 7(c). It is obvious that the main distribution

FIG. 8. Flowchart of the SA algorithm.

of the experimental retrieval agrees well with the theoretical result. For better comparison, we have plotted the results at time delays of 42.4 and 43 ps in Figs. 7(d) and 7(e). The solid and the dashed lines correspond to the retrieved and the calculated results, respectively. One can see that the overall agreement between the retrievals (solid line) and calculations (dashed line) is very good. From the experimental retrievals, we can also make a movie of the rotational dynamics of the CO_2 molecule. Besides, it is worth mentioning that the ADs of HHG from the CO_2 molecule is different from that of N_2. For instance, at the antialignment retrievals (e.g., $t = 42.4$ ps for CO_2 and $t = 8.2$ ps for N_2), HHG from CO_2 is peaked at $\alpha = 0°$ [see Fig. 7(a)], while it is $\alpha = 90°$ for N_2 [see Fig. 2(a)]. Such a difference in the harmonic ADs can be attributed to the different electronic structures of CO_2 and N_2, since the orientation-dependent electronic response is also convoluted in the HHG signals.

APPENDIX C: RETRIEVAL ALGORITHM FOR MOLECULAR ROTATION MOVIE

To make a movie of the molecular rotational dynamics, we have retrieved the complex coefficients $C_{JM,J'M'}$ for each initial rotational state $|JM\rangle$ from the angle-resolved HHG signals by using the simulated annealing (SA) algorithm, which is an efficient machine learning algorithm inspired from annealing in metallurgy for solving the global optimum problem [55,56]. Figure 8 shows the flowchart of the SA algorithm. The details of this algorithm are as follows:

(1) At the beginning, we set a random initial solution (both the amplitude and phase) of the coefficient for each initial rotational state, i.e., $x^{(0)} = |C_{JM,J'M'}^{(0)}| \exp[i\phi_{JM,J'M'}^{(0)}]$. Here the superscript in brackets refers to the iteration number.

(2)At each iteration step, we first calculate the ADs $I_q^{\text{cal}}[x^{(k)}]$ of the harmonic according to Eqs. (1)–(3), and evaluate the fitness of the solution $x^{(k)}$ by a cost function, which is given by the squared difference between the measured and calculated signals, i.e., $s^{(k)} = f[x^{(k)}] = |I_q^{\text{cal}(k)} - I_q^{\text{mea}(k)}|^2$.

(3) A neighboring solution $x'^{(k)}$ is generated by a generator function $\mathcal{N}[x^{(k)}, T^{(k)}]$, which is defined as $x'^{(k)} = \mathcal{N}[x^{(k)}, T^{(k)}] = x^{(k)} + \varepsilon\sqrt{T^{(k)}}$. Here ε is a random number ranging from 0 to 1, and $T^{(k)}$ is the so-called temperature in the SA algorithm at the kth iterative step [55,56]. The new solution $x'^{(k)}$ is also evaluated by calculating its cost function $s'^{(k)}$. We then evaluate these two solutions by comparing their cost functions:

(i) If $s'^{(k)}$ is smaller than $s^{(k)}$, which means the new generated solution is better than the old one, then the new generated solution is set to be the initial value of the next iteration step, i.e., $x^{(k+1)} = x'^{(k)}$ and $s^{(k+1)} = s'^{(k)}$.

(ii) If $s'^{(k)}$ is larger than $s^{(k)}$, which means the fitness quality of the new generated solution is deteriorated, then a transition probability function is defined, which is given by

$$p = \mathcal{P}[s^{(k)}, s'^{(k)}, T^{(k)}] = \frac{1}{1 + [s^{(k)} - s'^{(k)}]T^{(k)}}.$$

Meanwhile, the algorithm will generate a random number r ranging from 0 to 1. If $r > p$, the solution remains static, i.e., $x^{(k+1)} = x^{(k)}$, $s^{(k+1)} = s^{(k)}$. Otherwise, this worse solution will be assigned to the initial value of the next step, i.e., $x^{(k+1)} = x'^{(k)}$, $s^{(k+1)} = s'^{(k)}$. Such an operation can effectively eliminate the local minimum during the iteration.

The iteration is performed with the temperature reduced following $T^{(k)} = T_0 \times 0.95^k$, where initial temperature T_0 is set to be 10 000 K in our retrieval. The SA algorithm will not stop reducing the temperature and redoing the iteration until the stop condition is met. In our work, the stop condition is set to $s < 10^{-6}$ so that the obtained solution can well reproduce the experimental results. With the SA algorithm, we have successfully retrieved the complex coefficient $C_{JM,J'M'}$

for each initial rotational state. The experimental retrievals are demonstrated to agree well with the theoretical results (see Figs. 3 and 4). Note that we have also performed the retrievals with some other global optimization algorithms of machine learning, such as the particle swarm optimization [57]. The retrievals are in good agreement with the SA results.

APPENDIX D: THEORETICAL METHODS OF HHG FROM ROTATIONAL MOLECULES

To compare with the experiment, we have also simulated the molecular rotational dynamics by solving the time-dependent Schrödinger equation (TDSE) of the molecular RWP. For each initial rotational state $|JM\rangle$, the TDSE reads [48–51]

$$i\frac{\partial \Psi_{JM}(\theta, \phi, t)}{\partial t} = \left[B_0 \mathbf{J}^2 - \frac{E^2(t)}{2}(\alpha_\parallel \cos^2\theta \right.$$
$$\left. + \alpha_\perp \sin^2\theta) \right] \Psi_{JM}(\theta, \phi, t). \quad (\text{D1})$$

Here, $\mathbf{J}$ is the rotation operator, B_0 is the rotational constant of the N_2 molecule, and $\alpha_\parallel$ and $\alpha_\perp$ are the anisotropic polarizabilities in parallel and perpendicular directions with respect to the molecular axis, respectively. $E(t)$ is the envelope of the field vector of the pump pulse. Equation (D1) is solved with the split-operator method for each initial rotational state $|JM\rangle$ [58]. Assuming a Boltzmann distribution of the rotational levels at the initial time, the MAD at each time delay can be obtained in terms of Eq. (2). The harmonic spectrum is then calculated according to Eq. (3). In our simulations, the single-molecule response is calculated based on the QRS theory [10,51]. The intensity of the probe pulse is estimated from the harmonic cutoff in the experiment, which is about 2.3×10^{14} W/cm^2. The intensity of the pump pulse is determined by minimizing the squared difference between the measured and calculated HHG signals, which is about 1.1×10^{13} W/cm^2. Other parameters are the same as the experimental conditions.

[1] H. Ihee, V. A. Lobastov, U. M. Gomez, B. M. Goodson, R. Srinivasan, C. Y. Ruan, and A. H. Zewail, Science **291**, 458 (2001).

[2] A. H. Zewail and J. M. Thomas, *4D Electron Microscopy: Imaging in Space and Time* (Imperial College Press, London, 2009).

[3] O. Smirnova and M. Ivanov, Nat. Phys. **6**, 159 (2010).

[4] M. M. Seibert, T. Ekeberg, F. Maria, M. Svenda, J. Andreasson, O. Jönsson, D. Odić, B. Iwan, A. Rocker *et al.*, Nature **470**, 78 (2011).

[5] H. Chapman, P. Fromme, A. Barty, T. White, R. Kirian, A. Aquila, M. Hunter, J. Schulz, D. DePonte, U. Weierstall *et al.*, Nature **470**, 73 (2011).

[6] G. Sciaini and R. J. D. Miller, Rep. Prog. Phys. **74**, 096101 (2011).

[7] J. Küpper, S. Stern, L. Holmegaard, F. Filsinger, A. Rouzée, A. Rudenko, P. Johnsson, A. Martin, M. Adolph, A. Aquila *et al.*, Phys. Rev. Lett. **112**, 083002 (2014).

[8] P. B. Corkum, Phys. Rev. Lett. **71**, 1994 (1993).

[9] M. Lewenstein, Ph. Balcou, M. Ivanov, A. L'Huillier, and P. B. Corkum, Phys. Rev. A **49**, 2117 (1994).

[10] C. D. Lin, A. Le, Z. Chen, T. Morishita, and R. Lucchese, J. Phys. B **43**, 122001 (2010); L. Liang, P. Lan, X. Zhu, T. Huang, Q. Zhang, M. Lein, and P. Lu, Phys. Rev. Lett. **122**, 193901 (2019); J. P. Li, Q. Zhang, L. Li, X. Zhu, T. Huang, P. Lan, and P. Lu, Phys. Rev. A **99**, 033421 (2019).

[11] A. Tong, Q. Li, X. Ma, Y. Zhou, and P. Lu, Opt. Express **27**, 6415 (2019); X. Ma, Y. Zhou, Y. Chen, M. Li, Y. li, Q. Zhang, and P. Lu, *ibid.* **27**, 1825 (2019).

[12] M. Meckel, D. Comtois, D. Zeidler, A. Staudte, D. Pavičić, H. C. Bandulet, H. Pépin, J. C. Kieffer, R. Dörner, D. M. Villeneuve *et al.*, Science **320**, 1478 (2008).

[13] C. I. Blaga, J. Xu, A. DiChiara, E. Sistrunk, K. Zhang, P. Agostini, T. Miller, L. Dimauro, and C. D. Lin, Nature **483**, 194 (2012).

[14] J. Xu, C. I. Blaga, K. Zhang, Y. Lai, C. D. Lin, T. A. Miller, P. Agostini, and L. F. DiMauro, Nat. Commun. **5**, 4635 (2014).

[15] B. Wolter, M. G. Pullen, A.-T. Le, M. Baudisch, K. Doblhoff-Dier, A. Senftleben, M. Hemmer, C. D. Schröter, J. Ullrich, T. Pfeifer *et al.*, Science **354**, 308 (2016).

[16] Y. Huismans, A. Rouzée, A. Gijsbertsen, J. H. Jungmann, A. S. Smolkowska, P. S. W. M. Logman, F. Lépine, C. Cauchy, S. Zamith, T. Marchenko *et al.*, Science **331**, 61 (2011).

[17] K. Liu, S. Luo, M. Li, Y. Li, Y. Feng, B. Du, Y. Zhou, P. Lu, and I. Barth, Phys. Rev. Lett. **122**, 053202 (2019); Y.-N. Qin, M. Li, Y. Li, M. He, S. Luo, Y. Liu, Y. Zhou, and P. Lu, Phys. Rev. A **99**, 013431 (2019); R. Wang, Q. Zhang, D. Li, S. Xu, P. Cao, Y. Zhou, W. Cao, and P. Lu, Opt. Express **27**, 6471 (2019).

[18] M. Meckel, A. Staudte, S. Patchkovskii, D. M. Villeneuve, P. B. Corkum, R. Dörner, M. Spanner *et al.*, Nat. Phys. **10**, 594 (2014).

[19] J. Tan, Y. Zhou, M. He, Y. Chen, Q. Ke, J. Liang, X. Zhu, M. Li, and P. Lu, Phys. Rev. Lett. **121**, 253203 (2018); J. Tan, Y. Zhou, M. He, Q. Ke, J. Liang, Y. Li, M. Li, and P. Lu, Phys. Rev. A **99**, 033402 (2019); M. Li, H. Xie, W. Cao, S. Luo, J. Tan, Y. Feng, B. Du, W. Zhang, Y. Li, Q. Zhang *et al.*, Phys. Rev. Lett. **122**, 183202 (2019); Y. Liu, J. Tan, M. He, H. Xie, Y. Qin, Y. Zhao, M. Li, Y. Zhou, and P. Lu, Opt. Quant. Electron. **51**, 145 (2019); S. Luo, M. Li, W. Xie, K. Liu, Y. Feng, B. Du, Y. Zhou, and P. Lu, arXiv:1905.06162.

[20] S. Baker, J. S. Robinson, C. A. Haworth, H. Teng, R. A. Smith, C. C. Chirilă, M. Lein, J. W. G. Tisch, and J. P. Marangos, Science **312**, 424 (2006).

[21] P. M. Kraus, B. Mignolet, D. Baykusheva, A. Rupenyan, L. Horný, E. F. Penka, G. Grassi, O. I. Tolstikhin, J. Schneider, F. Jensen *et al.*, Science **350**, 790 (2015).

[22] H. J. Wörner, J. B. Bertrand, D. V. Kartashov, P. B. Corkum, and D. M. Villeneuve, Nature **466**, 604 (2010).

[23] W. Li, X. Zhou, R. Lock, S. Patchkovskii, A. Stolow, H. C. Kapteyn, and M. M. Murnan, Science **322**, 1207 (2008).

[24] P. Lan, M. Ruhmann, L. He, C. Zhai, F. Wang, X. Zhu, Q. Zhang, Y. Zhou, M. Li, M. Lein *et al.*, Phys. Rev. Lett. **119**, 033201 (2017); L. He, Q. Zhang, P. Lan, W. Cao, X. Zhu, C. Zhai, F. Wang, W. Shi, M. Li, X. Bian *et al.*, Nat. Commun. **9**, 1108 (2018).

[25] J. Itatani, J. Levesque, D. Zeidler, H. Niikura, H. Pépin, J. C. Kieffer, P. B. Corkum, and D. M. Villeneuve, Nature **432**, 867 (2004).

[26] S. Haessler, J. Caillat, W. Boutu, C. Giovanetti-Teixeira, T. Ruchon, T. Auguste, Z. Diveki, P. Breger, A. Maquet, B. Carré *et al.*, Nat. Phys. **6**, 200 (2010).

[27] C. Vozzi, M. Negro, F. Calegari, G. Sansone, M. Nisoli, S. De Silvestri, and S. Stagira, Nat. Phys. **7**, 822 (2011).

[28] X. Wang, A. Le, Z. Zhou, H. Wei, and C. D. Lin, Phys. Rev. A **96**, 023424 (2017).

[29] K. Yoshii, G. Miyaji, and K. Miyazaki, Phys. Rev. Lett. **106**, 013904 (2011).

[30] V. Makhija, X. Ren, D. Gockel, A. Le, and V. Kumarappan, arXiv:1611.06476.

[31] X. Ren, V. Makhija, A. Le, J. Troß, S. Mondal, C. Jin, V. Kumarappan, and C. Trallero-Herrero, Phys. Rev. A **88**, 043421 (2013).

[32] A. Sinha, J. Lee, S. Li, and G. Barbastathis, Optica **4**, 1117 (2017).

[33] A. Goy, K. Arthur, S. Li, and G. Barbastathis, Phys. Rev. Lett. **121**, 243902 (2018).

[34] Y. Taigman, M. Yang, M. Ranzato, and L. Wolf, In *2014 IEEE Conference on Computer Vision and Pattern Recognition* (IEEE, New York, 2014).

[35] U. S. Kamilov, I. N. Papadopoulos, M. H. Shoreh, A. Goy, C. Vonesch, M. Unser, and D. Psaltis, Optica **2**, 517 (2015).

[36] M. W. Libbrecht and W. S. Noble, Nat. Rev. Genet. **16**, 321 (2015).

[37] J. Carrasquilla and R. G. Melko, Nat. Phys. **13**, 431 (2017).

[38] P. Raccuglia, K. Elbert, P. Adler, C. Falk, M. Wenny, A. Mollo, M. Zeller, S. Friedler, J. Schrier, and A. Norquist, Nature **533**, 73 (2016); J. W. Chen, K. Wang, H. Long, X. Han, H. Hu, W. Liu, B. Wang, and P. Lu, Nano Lett. **18**, 1344 (2018); W. W. Liu, X. Li, Y. Song, C. Zhang, X. Han, H. Long, B. Wang, K. Wang, and P. Lu, Adv. Funct. Mater. **28**, 1707550 (2018).

[39] H. Stapelfeldt and T. Seideman, Rev. Mod. Phys. **75**, 543 (2003).

[40] O. Ghafur, A. Rouzée, A. Gijsbertsen, W. Siu, S. Stolte, and M. J. J. Vrakking, Nat. Phys. **5**, 289 (2009).

[41] Y. Ohshima and H. Hasegawa, Int. Rev. Phys. Chem. **29**, 619 (2010).

[42] K. Lin, I. Tutunnikov, J. Qiang, J. Ma, Q. Song, Q. Ji, W. Zhang, H. Li, F. Sun, X. Gong *et al.*, Nat. Commun. **9**, 5134 (2018).

[43] E. T. Karamatskos, S. Raabe, T. Mullins, A. Trabattoni, P. Stammer, G. Goldsztejn, R. Johansen, K. Długołęcki, H. Stapelfeldt, M. J. J. Vrakking *et al.*, arXiv:1807.01034.

[44] R. N. Zare, Science **279**, 1875 (1998).

[45] B. K. McFarland, J. P. Farrell, P. H. Bucksbaum, and M. Gühr, Science **322**, 1232 (2008).

[46] A. T. Le, R. R. Lucchese, and C. D. Lin, J. Phys. B **42**, 211001 (2009).

[47] S. Fleischer, Y. Khodorkovsky, Y. Prior, and Ilya Sh. Averbukh, New J. Phys. **11**, 105039 (2009).

[48] K. Lin, Q. Song, X. Gong, Q. Ji, H. Pan, J. Ding, H. Zeng, and J. Wu, Phys. Rev. A **92**, 013410 (2015).

[49] K. Lin, P. Lu, J. Ma, X. Gong, Q. Song, Q. Ji, W. Zhang, H. Zeng, J. Wu, G. Karras, G. Siour, J.-M. Hartmann, O. Faucher, E. Gershnabel, Y. Prior, and I. Sh. Averbukh, Phys. Rev. X **6**, 041056 (2016).

[50] L. He, P. Lan, A. Le, B. Wang, B. Wang, X. Zhu, P. Lu, and C. D. Lin, Phys. Rev. Lett. **121**, 163201 (2018).

[51] A. T. Le, R. R. Lucchese, S. Tonzani, T. Morishita, and C. D. Lin, Phys. Rev. A **80**, 013401 (2009).

[52] See Supplemental Material at http://link.aps.org/supplemental/10.1103/PhysRevA.99.053419 for the retrieved and simulated rotation movie of N_2.

[53] K. Yoshii, G. Miyaji, and K. Miyazaki, Opt. Lett. **34**, 1651 (2009).

[54] L. He, P. Lan, Q. Zhang, C. Zhai, F. Wang, W. Shi, and P. Lu, Phys. Rev. A **92**, 043403 (2015).

[55] S. Kirkpatrick, C. D. Gelatt, and M. P. Vecchi, Science **220**, 671 (1983).

[56] P. J. Van Laarhoven and E. H. Aarts, *Simulated Annealing* (Springer, New York, 1987).

[57] J. Kennedy, and R. Eberhart, in *1995 IEEE International Conference on Neural Networks* (IEEE, New York, 1995).

[58] S. Saugout, E. Charron, and C. Cornaggia, Phys. Rev. A **77**, 023404 (2008).